Peng et al. Intermetallics, 142 (2022), https://doi.org/10.1016/j.intermet.2022.107465

Al-Mn-Fe intermetallic formation in AZ91 magnesium alloys: effects of impurity iron

L. Peng[a,c], G. Zeng[b], J. Xian[a], C.M. Gourlay[a,d]

[a] Department of Materials, Imperial College London, London. SW7 2AZ. UK

[b] School of Materials Science and Engineering, Central South University, Changsha 410083, China

[c] email: liuqing.peng15@imperial.ac.uk

[d] email: c.gourlay@imperial.ac.uk

Abstract

The influence of iron on the formation of Al-Mn-Fe intermetallic compounds (IMCs) has been investigated in the solidification of Mg-9Al-0.7Zn-0.2Mn (wt.%, AZ91) with iron contents ranging from ~0.001 to > 0.01 wt.% Fe. Four Al-Mn-Fe IMCs formed depending on the Fe-content and location in the crucible: B2-Al(Fe,Mn), Al_8Mn_5, $Al_{11}Mn_4$ and, at the bottom of crucibles, Al_5Fe_2. The four IMCs nucleated and grew on one another, producing multiphase particles. These usually contained numerous orientations that were all interrelated through simple orientation relationships that are discussed in terms of the similarities between the IMC crystal structures. The iron content affected the IMC phase fractions and the multiphase particle morphology. At low iron content, the Fe-rich B2 phase was encapsulated by a low-Fe Al_8Mn_5 shell. With increasing iron content, the Fe-rich phases (B2 and Al_5Fe_2) gradually became in direct contact with the α-Mg. The threshold Fe:Mn content for adequate corrosion performance is found to correlate approximately to where B2-Al(Fe,Mn) first becomes exposed to the α-Mg matrix.

Keywords: Intermetallics; Nucleation and growth; Casting; Microstructure; Electron backscatter diffraction; Automotive uses.

1 Introduction

Magnesium-aluminium-based alloys (e.g., AZ and AM series alloys) are the most widely used Mg alloys in the automotive industry for lightweighting while providing adequate strength (e.g., AZ91) and ductility (e.g., AM50) [1-4]. However, they can suffer from poor corrosion performance when the level of impurity Fe, Ni and/or Cu is too high [5, 6] which is a barrier to the use of recycled Mg alloys. This is due to the low standard electrode potential of α-Mg compared with nobler elements [7] which causes α-Mg to corrode as the anode in the electrolytic reaction with cathodic secondary phases in the α-Mg matrix [7, 8].

Fe is the most common impurity which comes from magnesium reduction processes, master alloys and the steel containers/tools used in the Mg industry for melting, holding, ladling and casting. Extensive research has shown that the corrosion rate of Mg increases dramatically after a certain threshold Fe concentration [5, 6, 9, 10]. Later research [11-14] suggested the corrosion behaviour of Mg-Al-based alloys is closely related to the Al-Mn-Fe IMCs in direct contact with α-Mg. Lunder et al. [11] performed electrochemical tests for a range of Mn- and Fe-bearing IMCs in Mg-Al-based alloys. The results showed that (i) for binary Al-Mn IMCs (containing no Fe) the open circuit potential becomes larger with respect to α-Mg as the Mn content in the Al-Mn IMC increases: Al_8Mn_5>Al_4Mn>Al_6Mn>α-Mg, (ii) with only a few percent dissolved Fe in the Al-Mn IMCs the open circuit potential increases substantially away from the α-Mg; and (iii) Al_3Fe (also known as $Al_{13}Fe_4$) showed the largest potential difference to pure Mg of the IMCs studied.

To combat impurity Fe, alloying with manganese (Mn) has been adopted as a well-known method since the 1940s [15]. The Mn reacts with Al and impurity Fe in the Mg-Al melt and forms Al-Mn-Fe intermetallic compounds as primary solidification phases. These can settle to the bottom of crucibles [16] and remain there when the liquid is poured, hence the Fe content

can be controlled to an acceptable level [15]. The remaining low level of Fe solidifies within $Al_x(Mn,Fe)_y$ compounds that are much less damaging micro-cathodes than Mn-free Al_xFe_y compounds [12].

Excessive Mn can also increase the corrosion rate by forming Mn-rich Al-Mn compounds [9, 11]. Thus, the Mg industry has set a tolerance limit for the Mn, Fe and Fe/Mn ratio for specific alloys. For example, in the ASTM B94-18 standard [17] the Fe content in AZ91D shall not exceed 0.005 wt.% (50 ppm), and the Mn content shall be within 0.15-0.5 wt.%; and if either the minimum Mn limit or the maximum Fe limit is not met, the Fe/Mn ratio shall not exceed 0.032.

Chen et al. [18] studied AZ91 alloys with Mn content lower than the tolerance limit (0-0.1 wt.% Mn), and showed through EDS and thermodynamic calculations the formation of the Fe-rich phases Al_5Fe_2, Al_2Fe and BCC-B2. Although these IMCs were not studied by Lunder et al. [11, 12], it is likely that each will act as damaging micro-cathodes to the α-Mg matrix since they all have a lower Al content and higher Fe content than $Al_{13}Fe_4$.

For alloys containing sufficient Mn, the mechanisms behind the Fe tolerance limit for Mg-Al alloys have not been conclusively established [19]. Liu et al. [20] compared corrosion data with calculated phase diagrams and suggested that the Fe tolerance limit could correlate with the formation of the Fe-rich phase BCC-B2-Al(Fe,Mn). However, later Zeng et al. [21] showed that even for high-purity AZ91 containing ~10-30 ppm Fe with 0.15 wt.% Mn, which is within the Fe tolerance limit, the B2-Al(Fe,Mn) phase was present. Gandel et al. [22] revealed an Fe particle encapsulated by a layer of Mn which was not expected in CALPHAD analysis (equilibrium thermodynamics). Although this Mn-Fe particle was in a Mg-Zr-Fe alloy, it indicates that a microstructural analysis is necessary to understand the complexity of Fe-containing particles and how the tolerance limit is related to the Al-Mn-Fe phases.

Past work by Han et al. [23] revealed the Al-Mn-Fe IMC particles formed with different amounts of $FeCl_3$ addition, and identified the metastable phase τ-$Al_{0.89}Mn_{1.11}$ in low Al and Fe alloys (AZ31 and AZ61 without $FeCl_3$ addition). An Fe-rich core of Fe(Al) was detected in Al_8Mn_5 particles. This work further highlights the need to systematically understand how the Fe impurity level affects the microstructure of Al-Mn-Fe phases.

Based on the uncertainties outlined above, there is a need for a detailed microstructural study on (i) the formation of Al-Mn-Fe IMCs in AZ91 contaminated with Fe, (ii) how the IMC microstructure changes with varying Fe content, and (iii) how the changing Al-Mn-Fe IMC phases and microstructure correlate with the corrosion tolerance limit.

2 Methods

The strategy adopted to study the influence of Fe content on the formation of Al-Mn-Fe intermetallics in AZ91 was to hold a small size (2 g) of AZ91 in uncoated steel crucibles at different temperatures above the liquidus of α-Mg to allow the melt to pick up Fe, followed by solidification. Fig. 1a illustrates the equilibrium phase diagram for the saturated Fe content in the alloy at different target temperatures, plotted using Pandat software with the PanMg2018 database. The black dashed lines indicate the change in liquid composition during Fe pickup at each holding temperature. The maximum Fe content in the liquid assuming uniform saturation of the melt is given by the diamonds at each temperature. With this approach, Fe contents up to ~200 ppm (0.02 wt.%) could be reached according to Fig. 1a.

The starting material for this study was AZ91D with composition given in Table I. 2-g AZ91 cylinders were cut directly from this ingot and a steel bar was machined into mild steel crucibles with dimensions of inner diameter of 12 mm and inner height of 20 mm. The composition of the steel is given in Table II. The AZ91 cylinders were melted and held in the steel crucibles at 640-850 °C for 4 h, within sealed silica glass tubes backfilled with Ar. After the desired holding time, the samples were solidified by placing the hot glass tubes in the vertical cylindrical hole of a steel mould at room temperature. The cooling rate in the range of 700-400 °C was measured as ~4 K/s.

Table I Chemical composition of the AZ91 used in the experiment.

Alloy	**Composition (wt.%)**							
AZ91	Mg	Al	Zn	Mn	Cu	Si	Ni	Fe
	Bal.	8.95	0.72	0.19	0.001	0.039	<0.001	<0.001

Table II Chemical composition of the mild steel crucible used in the experiment.

Alloy	**Composition (wt.%)**					
	Fe	C	Mn	Si	P	S
Fe-0.2C	Bal.	0.2	0.7	0.35	<0.05	<0.05

The microstructure of Al-Mn-Fe IMC particles was examined by analytical scanning electron microscopy (SEM). Cross-sections were prepared by standard metallographic procedures but with ethanol instead of water and, immediately after polishing, SEM investigation was performed using a Zeiss Sigma-300. To reveal the 3-D morphology of IMC particles, the samples were etched in 10% nitric acid in ethanol for 5-10 minutes to selectively dissolve the α-Mg. Secondary electron (SE) and backscattered electron (BSE) images were taken with an accelerating voltage of 10 kV and a working distance of 10 mm. Energy-dispersive X-ray spectroscopy (EDS) was performed using an accelerating voltage of 10 kV, a 60-μm aperture and a working distance of 5 mm with an OXFORD X-Max detector. Electron backscattered diffraction (EBSD) was carried out using 20 kV accelerating voltage and 15 mm working distance, with a 120-μm aperture, the sample tilted at 70°, and a Bruker e-FlashHR EBSD detector. For indexing of EBSD patterns, the phases that were considered in the Bruker Quantax Esprit 2.1 and Bruker DynamicS software are listed in Table III along with their crystallographic details and references to the original crystallographic studies.

Table III Crystal structures and lattice parameters used for analysing and indexing EBSD patterns and XRD spectra. The structures from references [24-29] were assumed in this work.

Phase	**Space group**	**Pearson symbol**	**Lattice parameters**						**ICSD collection code**	**Ref.**
			a[Å]	b[Å]	c[Å]	α[°]	β[°]	γ[°]		
α-Mg	$P6_3/mmc$	*hP2*	3.209	3.209	5.211	90.0	90.0	120.0	52260	[24]
Al(Fe,Mn)	$Pm\bar{3}m$	*cP2*	2.910	2.910	2.910	90.0	90.0	90.0	165164	[25]
Al_8Mn_5	$R3mH$	*hR26*	12.674	12.674	7.946	90.0	90.0	120.0	254155	[26]
$Al_{11}Mn_4$	$P\bar{1}$	*aP15*	5.095	8.879	5.051	89.4	100.0	105.0	10509	[27]
Al_5Fe_2	$Cmcm$	*oS15*	7.656	6.415	4.218	90.0	90.0	90.0	105132	[28]
$Mg_{17}Al_{12}$	$I\bar{4}3m$	*cI58*	10.544	10.544	10.544	90.0	90.0	90.0	23607	[29]

The phases in the reaction layer with the steel crucible were identified further by X-ray diffraction (XRD) using a Bruker D2 Phaser diffractometer with a Lynx-Eye detector and Cu Kα radiation (λ = 1.5418 Å). XRD was performed on the surface of the reaction layer after α-Mg was selectively etched away in 20% nitric acid in ethanol. The solid sample was rotated at 60 rpm and the diffraction data were collected in the 2θ range of 10-90° with an angular step size of 0.02° and 1-3.5 s integration time.

3 Results and discussion

3.1 Summary of key features

Fig. 1b overviews the typical microstructure of AZ91 in an Fe-0.2C crucible after isothermal holding at 700 °C for 4 h. The eutectic $Mg_{17}Al_{12}$ and Al-Mn-Fe intermetallic compounds (IMCs) are highlighted in the α-Mg matrix. Between the α-Mg matrix and the crucible, a continuous IMC reaction layer can be observed.

3.2 Phase identification

Four different Al-Mn-Fe IMCs were identified in AZ91 depending on the Fe content: Al_8Mn_5, $Al_{11}Mn_4$, B2-Al(Fe,Mn) (i.e., with CsCl structure, Table III) and Al_5Fe_2. Fig. 2 displays EBSD analysis of two particles which contain these four IMCs. Our concern in this section is to identify and distinguish between these phases; the next sections consider the conditions for their formation and microstructure development. Fig. 2a and b show EBSD phase maps based on Hough-transform auto-indexing in Bruker Esprit using the phases in Table III. Experimental Kikuchi patterns from these maps are shown in Fig. 2c for each phase, highlighted with the same colour scheme used in the EBSD phase maps. To confirm the indexing further and test for the likelihood of phase misindexing, dynamical simulations were performed in Bruker DynamicS. Examples are given in Fig. 2c along with cross correlation coefficients (CCCs) between the simulated and experimental patterns. Visual band-by-band inspection shows good consistency between the measured and simulated Kikuchi patterns. Similar dynamical simulations and cross correlation analysis was performed to inter-compare the four IMCs. The results are given in Table IV, where it can be seen that the phases (and orientations) determined by Hough-based auto-indexing are in good agreement with the best-fitting dynamical simulations. The simulation patterns are given in S.I.-Fig. 1 in supplementary information.

Importantly, the CCC values are substantially higher for the correct phase compared to the other candidate phases in each case. This confirms that these four phases could be easily distinguished by EBSD using the Hough transform method and, therefore, most of this study was conducted with Hough-based auto-indexing.

Table IV Cross correlation coefficients between four experimental Kikuchi patterns autoindexed as four IMCs (column titles), and dynamical simulations of the four IMCs (row titles). Bold text highlights the best matching phase to each experimental pattern.

		Experimental Kikuchi patterns phases from Hough-based auto indexing			
		B2	Al_8Mn_5	$Al_{11}Mn_4$	Al_5Fe_2
Dynamical simulations	B2	**0.79**	0.38	0.15	0.24
	Al_8Mn_5	0.41	**0.73**	0.17	0.23
	$Al_{11}Mn_4$	0.33	0.19	**0.75**	0.24
	Al_5Fe_2	0.34	0.17	0.23	**0.78**

The same IMCs also formed as reaction layers on the steel crucible surface (Fig. 1b) and were suitable for XRD analysis. Fig. 2d shows the XRD patterns for the top surface of the reaction layer after α-Mg was selectively etched away. A two-phase mixture of Al_8Mn_5 and B2-Al(Fe,Mn) was identified for the as-etched surface in 700 °C samples and a two-phase mixture of Al_5Fe_2 and B2-Al(Fe,Mn) was identified in 750 °C samples. The phases B2-Al(Fe,Mn), Al_8Mn_5 and Al_5Fe_2 identified in the reaction layers by XRD are consistent with the indexed phases in the EBSD analysis. $Al_{11}Mn_4$ was not detected by XRD due to a small volume fraction of $Al_{11}Mn_4$ formed on the top of the reaction layer. The different backgrounds for the two XRD results in Fig. 2d are likely due to the roughness of the as-etched surface and the Fe composition in the IMC layers (Fe fluorescence). Note that no background correction has been applied so as to present the raw collected data.

Table V displays EDS point analysis results for the chemical composition of the IMC particles that were randomly measured at different locations of the sample: at the bottom of the crucible, in the middle of the bulk and at the top of the bulk. The average and standard deviation are

given for each phase. It can be seen that the Fe content in B2-Al(Fe,Mn) increased significantly with increasing holding temperature from 700 to 800 °C and maximized at ~43 at.% Fe in 800 and 850 °C, whereas the Al content in B2-Al(Fe,Mn) remained at ~45 at.% across the whole temperature range. Note that, after holding at 700 °C, the B2-Al(Fe,Mn) contained more Mn than Fe whereas, after holding at 800 °C, the B2-Al(Fe,Mn) contained more Fe than Mn. On the other hand, the composition of Al_8Mn_5, Al_5Fe_2 and $Al_{11}Mn_4$ remained at a similar level at all holding temperatures. The Al_8Mn_5 had up to ~10 at.% dissolved Fe whereas $Al_{11}Mn_4$ had significantly less dissolved Fe. The measured composition of the IMC phases are in good agreement with the recent thermodynamic calculations of the Al-Mn-Fe system in Ref. [30].

Table V EDS point measurements for IMC phases in the AZ91 held at different temperatures.

Phase	**Holding temperature [°C]**	**Composition**		
		Al [at.%]	**Mn [at.%]**	**Fe [at.%]**
B2-Al(Fe,Mn)	700	45±1	34±3	21±3
B2-Al(Fe,Mn)	750	44±1	20±3	36±3
B2-Al(Fe,Mn)	800-850	44±2	13±4	43±4
Al_8Mn_5	700-850	53±2	41±2	6±3
$Al_{11}Mn_4$	700-850	66±2	32±1	2±1
Al_5Fe_2	750-850	66±1	3±2	31±2

3.3 Morphology of Al-Mn-Fe IMCs

Fig. 3a summarises the typical changes in the morphology of Al-Mn-Fe IMC particles as the Fe content was increased by increasing the holding temperature in steel crucibles from 640 to 850 °C for 4 h. The left column in Fig. 3a displays SE images of the 3-D morphology after deep-etching; the middle column displays the cross-section of a selected IMC particle which has a similar shape to the 3-D particle; the right column is the EBSD phase map corresponding to the cross-section in the middle column. Fig. 3b plots the percentage of the IMC morphologies in Fig. 3a measured in 85 BSE images (400x magnification). The total count of measured particles is marked in the rectangular bar for each temperature (e.g., 165 Al-Mn-Fe IMC particles were studied in samples held at 700 °C).

It can be seen in Fig. 3 that at low Fe content (640 °C), the particles were equiaxed multifaceted single-phase Al_8Mn_5 which is consistent with the equilibrium calculation in Fig. 1a. Past work has shown these multifaceted particles have at least three facet families [21, 31]. As the Fe content increased (700 °C), a B2-Al(Fe,Mn) core became visible in cross-sectioned Al_8Mn_5 particles but the overall morphology of Al_8Mn_5 remained a similar multifaceted polyhedron. As the Fe content increased further (750 °C), the B2-Al(Fe,Mn) core grew larger and Al_8Mn_5 growing off the B2 developed an octapod form. Additionally, cube-shaped particles started to appear in the microstructure from 750 °C. EBSD in Fig. 3 shows that these cubes are comprised of large B2-Al(Fe,Mn) cores and a thin layer of Al_8Mn_5. At higher Fe content (800 °C), more cube-shaped particles formed and octapods contained larger dendritic B2-Al(Fe,Mn) cores. At the highest Fe content studied in this work (850 °C), the B2-Al(Fe,Mn) grew into large <111> dendrites up to ~80 μm long with Al_8Mn_5 growing on the B2 dendrite arms. Here the B2 core is so large that the overall particle shape is similar to the B2 dendrite shape. It can also be seen in Fig. 3 that, as the Fe content increases (holding temperature increases), the B2-Al(Fe,Mn)

phase has a relatively thinner shell of Al_8Mn_5 and, at the highest Fe contents, some B2 was in direct contact with α-Mg.

Note that eutectic Al_8Mn_5 rods (e.g. in [21]) and $Al_{11}Mn_4$ plates (e.g. in [31]) also grew off the multiphase particles but are not considered in this paper because they did not contain any Fe-rich phase.

Fig. 3 gives examples of the typical Al-Mn-Fe particles in the bulk AZ91, away from the bottom of the crucibles. The results at the bottom of crucibles were somewhat different, where Al_5Fe_2 phase also formed on IMC particles for holding temperatures in the range 750-850 °C. An example of Al_5Fe_2 growing on a cube particle is given in Fig. 2b. Al_5Fe_2 was only found at the bottom of crucibles and the chance of finding Al_5Fe_2 (volume fraction) significantly increased from 800 to 850 °C samples. In 850 °C, Al_5Fe_2 was very common on the B2 dendrites located within ~300 μm of the bottom, and gradually disappeared in the dendrites further away from the bottom. In the main bulk of the AZ91, Al_5Fe_2 was never observed in this work.

Fig. 4a quantifies the dimensions of Al-Mn-Fe IMC particles in AZ91 held at different temperatures, measured from 24 cross-section BSE images. For multifaceted, octapod, and cube particles and their B2-Al(Fe,Mn) core (Fig. 3), the particle dimension was converted into an equivalent circle diameter. For B2 dendrites in 850 °C samples (Fig. 3), the dimension was estimated as the dendrite envelope. Fig. 4b shows the area fraction of B2-Al(Fe,Mn) to the total area of the particle/dendrite. In Fig. 4a the overall particle dimension (dark blue) from 640 to 800 °C increases slightly from ~7-10 μm and then increases substantially at 850 °C to ~50 μm dendrites. The dimension of B2-Al(Fe,Mn) cores (red) also increases gradually from 700 to 800 °C but still within the Al_8Mn_5 particles until it dominates the overall size of the IMC particles at 850 °C. Although at this point the size of B2-Al(Fe,Mn) phase is almost the same size as the overall dendrite, other phases (Al_8Mn_5, Al_5Fe_2 or $Al_{11}Mn_4$) still grow on the dendrite

arms leading to a ~55% area fraction of B2-Al(Fe,Mn) to the overall dendrite at 850 °C in Fig. 4b.

Fig. 4c plots the calculated mass fraction of only the Mn- and Fe-bearing IMCs formed using the Scheil model in Pandat with the PanMg2018 database. It is assumed that each sample is uniformly saturated in Fe at the start temperature, with saturated Fe contents obtained from the equilibrium calculation in Fig. 1a. Fig. 4d is a similar plot but the Mn content in the alloy is reduced from 0.19 to 0.15 wt.%. In both Fig. 4c and d, the solid horizontal lines mark the temperature at which α-Mg begins to form, neglecting any nucleation undercooling, and the dashed line at lower temperature is the start of the $Mg_{17}Al_{12}$-containing eutectic reaction.

In Fig. 4c, at 640°C, Al_8Mn_5 is the only IMC phase stable above the liquidus of α-Mg; Al_8Mn_5 then continues forming with α-Mg across a wide temperature range followed by $Al_{11}Mn_4$ and then Al_4Mn. At increasing Fe saturation temperature, the B2-Al(Fe,Mn) phase is calculated to form first before Al_8Mn_5 and the remaining solidification path is then similar to low-Fe samples. The mass fraction of B2-Al(Fe,Mn) increases with increasing Fe content in the melt while the other phases remain largely unchanged. These calculations are in reasonable agreement with the observations in Fig. 3 and the measurements in Fig. 4a-b, except that Al_4Mn was not detected in this work.

The plot in Fig. 4d, where the Mn content in the calculations was reduced to 0.15 wt.%, displays a similar result except that a small amount of Al_5Fe_2 additionally forms after B2-Al(Fe,Mn) and before Al_8Mn_5. Performing similar calculations with the PanMg 2018 database varying the compositions of Mn and Fe in the range 10-1000 ppm, it was calculated that Al_5Fe_2 only appears in the Scheil model when the Mn content is ≤ 0.15 wt.%; and Al_8Mn_5 always forms after B2-Al(Fe,Mn) (without any Al-Fe compounds) when the Mn content is > 0.15 wt.% even if the Fe content is high (1000 ppm). This implies that the formation of Al_5Fe_2 on particles at

the bottom region of the crucible in this work is likely to be due to a local depletion in Mn, either because of the growth of settled Al-Mn particles or the diffusion of Mn into the steel crucible, or both. Indeed, our recent paper [32] held AZ91 in similar crucibles and EDS line scanning showed some Mn diffusion into the steel. In recent research [18], AZ91 with lower Mn content (0.1 and 0 wt.% Mn) also formed settled Al_5Fe_2.

3.4 Crystallography of Al-Mn-Fe IMC growth

3.4.1 ORs between Al_8Mn_5 and B2-Al(Fe,Mn)

Previous work by Zeng et al. [21] has found that rhombohedral Al_8Mn_5 particles in AZ91 are usually cyclic twinned, consisting of four orientations related by ~90° rotations around three common $\langle 11\bar{2}0\rangle_{\mathrm{HEX}}$ axes with $\{2\bar{2}01\}_{\mathrm{HEX}}$ twin planes. This cyclic twin can be understood better when considering Al_8Mn_5 in the body centred rhombohedral (BCR) setting of Al_8Mn_5 with lattice parameters a = b = c = 9.029 Å, α = β = γ = 89.1° [33], which is pseudo-cubic with <1° rhombohedral distortion. In the BCR setting, the cyclic twin planes are $\{100\}_{\mathrm{BCR}}$ and the four orientations rotate ~90° around the $\langle 100\rangle_{\mathrm{BCR}}$ axes. Zeng et al. [21] also found that Al_8Mn_5 has a "pseudo-cube-on-cube" OR with B2-Al(Fe,Mn), named **OR-1** in this work, which can be written as:

$$\{1\bar{1}0\}_{\mathrm{Al8Mn5-BCR}} \parallel \{1\bar{1}0\}_{\mathrm{B2}} \,\&\, \langle 111\rangle_{\mathrm{Al8Mn5-BCR}} \parallel \langle 111\rangle_{\mathrm{B2}} \ (\textbf{OR-1})$$

In Zeng et al.'s work [21], B2-Al(Fe,Mn) cores were small and usually difficult to find due to a low Fe content in the high purity AZ91 used. In this work, the cyclic twin OR of Al_8Mn_5 and the **OR-1** between Al_8Mn_5 and B2-Al(Fe,Mn) were commonly measured in samples contaminated with Fe where there are large B2 cores that could be easily found. Additionally, another reproducible Al_8Mn_5-to-B2 OR was found here, named **OR-2**:

$$\{10\bar{1}\}_{\mathrm{Al8Mn5-BCR}} \parallel \{1\bar{1}0\}_{\mathrm{B2}} \,\&\, \langle 111\rangle_{\mathrm{Al8Mn5-BCR}} \parallel \langle 111\rangle_{\mathrm{B2}} \ (\textbf{OR-2})$$

Fig. 5a shows a typical multifaceted Al_8Mn_5 particle which contains a large B2-Al(Fe,Mn) core. According to the IPF-Y orientation map, the B2-core is a single crystal (one colour) and the single-phase Al_8Mn_5 has four orientations (colours) which are slightly interlaced with multiple linear interfaces. The cyclic twin OR of Al_8Mn_5 can be identified in the pole figures in Fig. 5b, where all four orientations (colours) overlap at each spot in the $\{100\}_{\mathrm{BCR}}$ (or $\{2\bar{2}01\}_{\mathrm{HEX}}$) pole figure, and each spot in the $\{1\bar{1}0\}_{\mathrm{BCR}}$ (or $\{11\bar{2}0\}_{\mathrm{HEX}}$) pole figure contains two overlapping

orientations (colours). Different from the "pseudo-cube-on-cube" **OR-1**, the spots in the $\{100\}_{\mathrm{BCR}}$ (or $\{2\bar{2}01\}_{\mathrm{HEX}}$) pole figure in Fig. 5b do not overlap with the $\{100\}$ of B2 and only the $\langle 111\rangle_{\mathrm{BCR}}$ (or $\langle 0001\rangle_{\mathrm{HEX}}$) direction from one Al_8Mn_5 orientation (light blue) overlaps with one of the $\langle 111\rangle$ directions of B2. In the $\{1\bar{1}0\}_{\mathrm{BCR}}$ (or $\{11\bar{2}0\}_{\mathrm{HEX}}$) of Al_8Mn_5, three of the $\{1\bar{1}0\}_{\mathrm{BCR}}$ from the light blue orientation overlap with three of the $\{110\}$ of B2 whereas, for the other three orientations, only one of the $\{1\bar{1}0\}_{\mathrm{BCR}}$ overlaps with one of the $\{110\}$ of B2, giving totally three of the $\{1\bar{1}0\}_{\mathrm{BCR}}$ from the four orientations overlapping with three of the $\{110\}$ of B2. These are highlighted in the pole figures with grey dashed circles. The colour in the pole figures of single-orientation B2-Al(Fe,Mn) has been replaced by black for better visual recognition. The pseudo-cubic orientation of cyclic twinned BCR-Al_8Mn_5 has ~60° misorientation to the cubic B2-Al(Fe,Mn) and their crystal orientations are visualized in the wire frames attached to the pole figures, plotted from the measured Euler angles.

The EBSD measured **OR-1** and **OR-2** can be understood further with the stereographic projections shown in Fig. 5c. For cubic B2-Al(Fe,Mn) to the left, the projection is centred on a $\langle 111\rangle_{\mathrm{B2}}$ and all $\langle 111\rangle_{\mathrm{B2}}$, $\{110\}_{\mathrm{B2}}$ and $\{100\}_{\mathrm{B2}}$ are plotted. The two stereographic projections of the cyclic twinned Al_8Mn_5 are plotted according to the two ORs. Four Al_8Mn_5 orientations are coloured as red, green, blue and yellow with the $[111]_{\mathrm{BCR-Al8Mn5}}$ of the red orientation at the centre (red triangle) and all $\langle 111\rangle_{\mathrm{BCR}}$, $\{110\}_{\mathrm{BCR}}$ and $\{100\}_{\mathrm{BCR}}$ of Al_8Mn_5 are plotted. Considering the combined cyclic twin as one pseudo-cubic orientation, it can be seen that **OR-1** is a pseudo-cube-on-cube relationship. **OR-2** is a 60° rotation around the red $[111]_{\mathrm{BCR-Al8Mn5}}$ at the centre, which keeps the $\{1\bar{1}0\}_{\mathrm{BCR-Al8Mn5}}$ spots at the circumference parallel with the B2, but the $\{100\}_{\mathrm{BCR-Al8Mn5}}$ and the inner $\{1\bar{1}0\}_{\mathrm{BCR-Al8Mn5}}$ spots are no longer parallel with the same planes in B2. Note that **OR-2** involves a pseudo-cube to cube OR to the Σ3 twin to B2. Thus, **OR-1** and **OR-2** can be considered reverse-observe twins of each other.

This is also similar to a well-known twin law in cubic crystals, including the spinel contact twin and the fluorite penetration twin, although in those cases the two orientations are from the same phase. 32 out of 32 Al_8Mn_5 particles studied in this work were cyclic twinned. **OR-1** with B2 was measured in 19/32 (59%) particles while **OR-2** was measured in 12/32 particles (38%) and 1/32 particle had **OR-1** and **OR-2** coexisting.

3.4.2 ORs between $Al_{11}Mn_4$ and B2-Al(Fe,Mn)

Fig. 6a shows a cross-section of an Al_8Mn_5 octapod held at 800 °C for 4 h, containing a dendritic B2-Al(Fe,Mn) core and $Al_{11}Mn_4$ plates attached to the particle. The $Al_{11}Mn_4$ plates are in direct contact with B2-Al(Fe,Mn) in the grooves of the multiphase particle. Two orientation relationships were found between $Al_{11}Mn_4$ and B2-Al(Fe,Mn) in this work, named as **OR-I** and **OR-II**. Both ORs and multiple variants exist between different $Al_{11}Mn_4$ plates and one B2 dendrite. In Fig. 6b, two $Al_{11}Mn_4$ orientations were selected to show one of the variants in each OR. In **OR-I** the $\{010\}_{Al11Mn4}$, $\{011\}_{Al11Mn4}$ and $\{01\bar{1}\}_{Al11Mn4}$ are near-parallel to different members of $\{110\}_{B2}$ with $\langle 100\rangle_{Al11Mn4} \parallel \langle 111\rangle_{B2}$ marked in grey dashed circles. In **OR-II** the $\{010\}_{Al11Mn4}$, $\{2\bar{3}0\}_{Al11Mn4}$ and $\{210\}_{Al11Mn4}$ are near-parallel to different members of $\{110\}_{B2}$ with $\langle 00\bar{1}\rangle_{Al11Mn4} \parallel \langle 111\rangle_{B2}$ marked in grey dashed triangles. The crystal orientations can be seen in the unit cell wire frames attached to the pole figures with highlighted common planes. Note that the orientations of the Al_8Mn_5 in the IPF-Z map are not shown here for clarity (here the Al_8Mn_5 is cyclic twinned with **OR-1** with the B2).

At the right-hand side of Fig. 6a, three $\{010\}_{Al11Mn4}$ pole figures are given for four $Al_{11}Mn_4$ orientations (no.1-4) marked with the projected facet plane normal, showing that the $Al_{11}Mn_4$ plate facet is consistent with $\{010\}$ in each case and the different $Al_{11}Mn_4$ plates (no. 1-4) are parallel with the different members of $\{110\}_{B2}$ in Fig. 6b. This orientation relationship can be clearly confirmed in the deep etched images in Fig. 7 where the $Al_{11}Mn_4$ plates pass through one or multiple $\{110\}$ planes of the cube-shaped particles (which has similar shape of the underlying B2-cube, Fig. 3). In the Al_8Mn_5 octapods in Fig. 7, a similar OR with the $Al_{11}Mn_4$ plates can be observed if we consider the cubic symmetry of an octapod.

The multiple near-parallel planes in **OR-I** and **OR-II** can be understood better with the stereographic projections in Fig. 6c, where the $[111]_{B2}$, $[100]_{Al11Mn4}$ for **OR-I** and

$[001]_{Al11Mn4}$ for **OR-II** are aligned at the centre. Each plane family is assigned one colour. The angles between the planes at the circumference of the $Al_{11}Mn_4$-projections indicate that these marked planes cannot all be parallel to $\{110\}_{B2}$ at the same time and choosing different pairs of parallel planes changes the OR. However, the angular deviations are small (≤ 1.7°) and to a reasonable approximation all the $Al_{11}Mn_4$ planes in each stereogram can be considered to be near-parallel with the $\{110\}_{B2}$.

In Fig. 6, there are totally 10 $Al_{11}Mn_4$ orientations in the particle with 7 orientations in **OR-I** and 3 orientations in **OR-II**, with $\{010\}_{Al11Mn4}$ parallel with different members of the $\{110\}_{B2}$ family. As the Al_8Mn_5 has the "pseudo-cube-on-cube" **OR-1** with the B2-Al(Fe,Mn), the $Al_{11}Mn_4$ also has **OR-I** and **OR-II** equivalently to the BCR-Al_8Mn_5. But note that in body centred rhombohedral the $\{110\}_{BCR-Al8Mn5}$ is not symmetrically equivalent to the $\{1\bar{1}0\}_{BCR-Al8Mn5}$.

There are numerous near-parallel planes in **OR-I** and in **OR-II**, but the simplest way to write the ORs is:

$\{0\bar{1}0\}_{Al11Mn4} \parallel \{\bar{1}10\}_{B2}$ & $\langle 100\rangle_{Al11Mn4} \parallel \langle 111\rangle_{B2}$ (**OR-I**)

$\{010\}_{Al11Mn4} \parallel \{\bar{1}10\}_{B2}$ & $\langle 00\bar{1}\rangle_{Al11Mn4} \parallel \langle 111\rangle_{B2}$ (**OR-II**)

Our recent work on high-purity AZ91 measured different ORs between $Al_{11}Mn_4$ and Al_8Mn_5, showing that the presence of the B2-Al(Fe,Mn) phase affects the ORs between $Al_{11}Mn_4$ and Al_8Mn_5 in multiphase particles [31].

3.4.3 ORs between Al_5Fe_2 and B2-Al(Fe,Mn)

Fig. 8a shows a near-cube-shaped particle at the bottom of AZ91 held at 800 °C for 4 h. The nearly cubic B2-Al(Fe,Mn) core is surrounded by mostly Al_5Fe_2 and a little Al_8Mn_5. As the IPF-Y orientation map shows, the B2-Al(Fe,Mn) is a single crystal (one colour) and the Al_5Fe_2 has three different orientations (colours) at each side. They were all found to have the same orientation relationship to the B2 cube. For clarity, only the blue orientation in the IPF-Y map was plotted in the pole figures of Al_5Fe_2 in Fig. 8b where two of the $\{3\bar{1}1\}_{Al5Fe2}$, two of the $\{221\}_{Al5Fe2}$, one of the $\{130\}_{Al5Fe2}$ and the $\{001\}_{Al5Fe2}$ overlap with each spot in the $\{110\}_{B2}$ separately. Additionally, one of the $\langle 110\rangle_{Al5Fe2}$ and one of the $\langle 111\rangle_{B2}$ form a common direction, highlighted in grey dashed circles. Fig. 8c plots the stereographic projections for the multiple near-parallel planes shown in Fig. 8b with the common directions of $[111]_{B2}$ and $[110]_{Al5Fe2}$ aligned at the centre. In the projection of Al_5Fe_2, the same colour indicates the same family of planes and directions. The filled symbols are near-parallel in the OR, and unfilled symbols are other members of the plotted plane and direction families that are not parallel (see EBSD pole figures).

The OR found between Al_5Fe_2 and B2-Al(Fe,Mn) is in agreement with the OR between Al_5Fe_2 and A2-α-Fe (BCC with a = 2.866 Å [34]) which has been well studied in Fe-Zn hot-dip galvanizing with Al addition in the Zn bath [35-37] where Al_5Fe_2 forms on the A2-α-Fe substrate. Guttmann [35] reviewed the ORs as $(3\bar{1}1)_{Al5Fe2} \parallel (110)_{\alpha Fe}$ and $(221)_{Al5Fe2} \parallel (110)_{\alpha Fe}$. Recently, Wang et al. found the OR $(001)_{Al5Fe2} \parallel (0\bar{1}1)_{\alpha Fe}$ & $[110]_{Al5Fe2} \parallel [111]_{\alpha Fe}$ has a low misfit and it is likely to be the interface. This was later supported by Liu et al. [38], but written as $(002)_{Al5Fe2} \parallel (110)_{\alpha Fe}$ & $[1\bar{1}0]_{Al5Fe2} \parallel [1\bar{1}1]_{Al5Fe2}$.

The angles between the planes at the circumference of the Al_5Fe_2-projection are added as annotations in Fig. 8c. Since the angles are not exactly 60°, it is not possible for all these planes

in Al_5Fe_2 to be parallel to $\{110\}$ in B2 at the same time. Therefore, strictly, there are multiple ORs depending on which planes in Al_5Fe_2 are exactly parallel with $\{110\}$ in B2. However, all the plotted planes are nearly parallel with the $\{110\}_{B2}$ planes with a small degree of misorientation (<0.5°), and we treat them here as one OR. For simplicity and given that $\{001\}_{Al5Fe2}$ is most likely the interfacial plane, we write the OR between Al_5Fe_2 and B2 as:

$$\{001\}_{Al5Fe2} \parallel \{\bar{1}10\}_{B2} \,\&\, \langle 110\rangle_{Al5Fe2} \parallel \langle 111\rangle_{B2}$$

3.4.4 ORs between all IMCs

Fig. 9 shows a B2-Al(Fe,Mn) dendrite at the bottom region of the AZ91 held at 850 °C for 4 h, containing three visible dendrite arms in the cross-section image and the EBSD phase map. The Al_8Mn_5 and Al_5Fe_2 surround the primary/secondary arms of the B2 dendrite and the $Al_{11}Mn_4$ plates are around the tip of the primary arms. The IPF-Z orientation map is displayed for individual phases. The pole figures attached to the right display the $\{110\}$ and $\langle 111\rangle$ for B2-Al(Fe,Mn), the $\{1\bar{1}0\}_{\mathrm{BCR}}$ (or $\{11\bar{2}0\}_{\mathrm{HEX}}$) and $\langle 111\rangle_{\mathrm{BCR}}$ (or $\langle 0001\rangle_{\mathrm{HEX}}$) for Al_8Mn_5, the $\{001\}$ and $\langle 110\rangle$ for Al_5Fe_2, the $\{010\}$ and $\langle 100\rangle$ for $Al_{11}Mn_4$ with **OR-I** plus the $\{010\}$ and $\langle 001\rangle$ for $Al_{11}Mn_4$ with **OR-II**, showing the interrelationship between all IMCs discussed in the previous sections. All overlapped spots in the pole figures are marked in grey dashed circles for all IMCs.

It can be seen that the B2-Al(Fe,Mn) is a single crystal and the three dendrite arms in the cross-section are in $\langle 111\rangle$ directions indicating the B2 is a $\langle 111\rangle$-type dendrite. Another eight-arm $\langle 111\rangle$ dendrite can be seen in the 3-D image in Fig. 3. The Al_8Mn_5 has four orientations (colours) related by cyclic twinning and the "pseudo-cube-on-cube" **OR-1** to the B2-Al(Fe,Mn). The Al_5Fe_2 has 12 orientations (colours) growing on the B2-Al(Fe,Mn) with each individual orientation having the same OR as in Fig. 8. Each is a different variant of this OR. The $Al_{11}Mn_4$ has 9 orientations (colours) with **OR-I** and 7 orientations (colours) with **OR-II** with the B2-Al(Fe,Mn). All $\{010\}_{\mathrm{Al11Mn4}}$ are parallel with the different $\{110\}_{\mathrm{B2}}$ families for both **OR-I** and **OR-II**, but only a subset of possible variants is present.

Fig. 10 plots the stereographic projections for the EBSD-measured ORs for the four IMCs, where the shared common directions of the unit cells: $[111]$ in B2-Al(Fe,Mn), $[0001]$ in Al_8Mn_5, $[110]$ in Al_5Fe_2 and $[100]$ in **OR-I** of $Al_{11}Mn_4$ are located at the centre of the projections and aligned out of the screen. The corresponding atomic structure and unit cells are

plotted for each crystal to the left. The poles of the relevant common planes are shown in the stereographic projections using colour to indicate members of the same family in each crystal. Note that the higher Miller indices used, $\{33\bar{6}0\}_{\mathrm{HEX}}$ in Al_8Mn_5, $\{002\}$ in Al_5Fe_2 and $\{040\}/\{022\}$ in $Al_{11}Mn_4$, are chosen since these are the closest-packed planes in each crystal and all have similar d-spacings. The closest-packed planes are also shown in the atomic structures for each crystal with the same colour scheme as the poles in the stereographic projections. Note that all unit cells and atomic structures in Fig. 10 have been adjusted to the same scale and the d-spacing of the closest-packed planes are given in the middle. Note also that the unit cell and atomic structure of B2-Al(Fe,Mn) is drawn using parameters of binary B2-AlFe (Table III). The Mn present on the Fe lattice site slightly expands the d-spacing of the $\{110\}_{\mathrm{B2}}$ planes, e.g. 2.09 Å for a 0.6Mn and 0.4Fe occupation according to [39]. That is to say, the presence of Mn in B2-Al(Fe,Mn) is expected to make the $\{110\}_{\mathrm{B2}}$ d-spacing even closer to that of the planes in the other crystal structures.

It can be seen in Fig. 10 that all the relevant planes in Al_8Mn_5, Al_5Fe_2 and $Al_{11}Mn_4$ are parallel or nearly parallel with the six $\{110\}_{\mathrm{B2}}$ planes containing the shared common directions. The interplanar d-spacings and angles between the planes are remarkably similar and a good atomic match can be achieved between the four IMC crystals. This indicates the Al_8Mn_5, Al_5Fe_2 and $Al_{11}Mn_4$ could all individually nucleate and grow on the B2-Al(Fe,Mn) and the $Al_{11}Mn_4$ could also nucleate on the Al_8Mn_5 and Al_5Fe_2 in a similar way.

$Al_{11}Mn_4$ nucleated and grew on Al_5Fe_2 with a specific OR that is one permutation of the ORs implied between $Al_{11}Mn_4$ and Al_5Fe_2 in Fig. 10. To show this, Fig. 11 is a higher magnification microstructure of Al_8Mn_5, Al_5Fe_2 and $Al_{11}Mn_4$ on a B2 dendrite arm at the bottom of a crucible held at 850 °C for 4 h. In this example, a relatively high fraction of Al_5Fe_2 exists and some $Al_{11}Mn_4$ plates are growing on top of the Al_5Fe_2. The EBSD analysis in Fig. 11a was performed

before the cross-section was etched, and the BSE images of the dendrite arm after etching in Fig. 11b-d were taken at 0°, 40° and 54° tilted stage to reveal the 3-D microstructure of the IMCs underneath the cross-section.

In Fig. 11e, the $\{010\}$ pole figures for different $Al_{11}Mn_4$ orientations (colours) are given with marked plane normals to indicate the $\{010\}$ growth facet (as previously shown in Fig. 6 and Fig. 7). The $\{001\}$ pole figures of Al_5Fe_2 orientations contacting the $Al_{11}Mn_4$ plates are attached to the right. It can be seen in Fig. 11e that the $Al_{11}Mn_4$ grew on the Al_5Fe_2 with the orientation relationship of $\{010\}_{\mathrm{Al11Mn4}} \parallel \{001\}_{\mathrm{Al5Fe2}}$ with $[101]_{\mathrm{Al11Mn4}} \parallel [0\bar{1}0]_{Al5Fe2}$ in each case. Fig. 11f is a plot of the atomic structures of the $Al_{11}Mn_4$ and Al_5Fe_2 according to this OR, in projection view along the normal to $\{010\}_{\mathrm{Al11Mn4}} \parallel \{001\}_{\mathrm{Al5Fe2}}$. It can be seen that the atomic structures, including the pentagonal antiprisms, are closely related in this orientation relationship. The orthorhombic unit cell of Al_5Fe_2 (solid black rectangle) is highly similar to the red distorted rectangle in $Al_{11}Mn_4$ (with ~0.5° distortion and side-length differences 1.9% and 2.7%). The $Al_{11}Mn_4$ unit cell is shown in black and is almost a rhombus because $a \approx c$ (differing by <1%) in triclinic $Al_{11}Mn_4$, Table III. Note that all common directions in this alignment were confirmed by EBSD but only the pole figures for plane normals are shown here for space.

3.5 Implications for micro-galvanic corrosion

A key feature in the growth of multiphase Al-Mn-Fe particles in Fig. 3-Fig. 11 is that, as each new IMC forms in the solidification sequence, they nucleate on the pre-existing Al-Mn-Fe IMCs and grow to fully or partially cover them. This occurs due to the peritectic-like nature of the IMC formation reactions (Fig. 4c and d) and also due to the relatively good lattice matches caused by similarities between the IMC crystal structures (Fig. 10 and Fig. 11f). Combining these results and past corrosion studies (e.g. [11]), three factors are likely to determine the micro-galvanic corrosion performance of AZ91 with different levels of impurity Fe: (i) the IMC phases present in direct contact with α-Mg, (ii) their composition in terms of the Fe:Mn ratio in $Al_x(Mn,Fe)_y$, and (iii) the multiphase IMC particle microstructure.

Table VI summarizes the key microstructures of the IMCs, the saturated Fe content (Fig. 1a) and the Fe:Mn ratios in this work. The maximum allowable Fe/Mn ratio for high-purity AZ91D and AZ91E is 0.032 in the ASTM standards [17] [40], and the maximum allowable Fe content for both is 0.005 wt.% (50 ppm).

Table VI Saturation Fe content and Fe/Mn ratio for the AZ91 studied at different holding temperatures assuming the melt was uniformly saturated during isothermal holding.

Holding Temperature [°C]	Saturation Fe [wt.%]	Mn in the AZ91 [wt.%]	Fe/Mn ratio	Marks on morphology
640	0.0001	0.19	0.001	Equiaxed multifaceted Al_8Mn_5
700	0.0018	0.19	0.009	B2-Al(Fe,Mn) core encapsulated in multifaceted Al_8Mn_5
750	0.0044	0.19	0.023	B2-Al(Fe,Mn) core in multifaceted/octapod Al_8Mn_5; some Al_5Fe_2 on B2-cubes at the bottom of crucible
-	0.0061	0.19	0.032	(ASTM maximum Fe/Mn ratio for high purity AZ91D and AZ91E)
800	0.0094	0.19	0.050	B2-Al(Fe,Mn) core in octapod Al_8Mn_5; increased Al_5Fe_2 on B2-cubes at the bottom of crucible
850	0.0184	0.19	0.097	Large B2-Al(Fe,Mn) dendrites; massive Al_5Fe_2 on B2-dendrites at the bottom region of crucible

Note: maximum Fe limit for AZ91D and AZ91E: 0.005 wt.%

It can be seen in Table VI that the Fe content and Fe:Mn ratio does not exceed the limit of the ASTM standard for Fe contents associated with holding temperatures 640-750 °C whereas at 800 and 850 °C both Fe and the Fe/Mn ratio exceed the maximum limit. The maximum tolerable Fe content for the AZ91 containing 0.19 wt.% Mn is calculated in terms of the Fe:Mn ratio of 0.032 as 0.006 wt.% Fe, sitting somewhere between 750 and 800 °C marked in Fig. 1a. Comparing this with the results in Fig. 3 and Fig. 4, this Fe content (holding temperature) is where the octapod particles started to be dominant in the microstructure, B2-Al(Fe,Mn) cores tended to be only partially-covered by Al_8Mn_5 phase bringing them into direct contact with α-Mg, and the B2-Al(Fe,Mn) cubes with Al_5Fe_2 increased at the bottom of the crucible. An example of B2-Al(Fe,Mn) in direct contact with α-Mg is Fig. 2b, and more examples are given in S.I.-Fig. 2 in supplementary information.

Thus, it seems that the presence of B2-Al(Fe,Mn) phase is not the determining factor in corrosion performance of Fe-contaminated alloys since, at 700 °C, the B2-Al(Fe,Mn) phase was present yet the Fe content and Fe:Mn ratio were both well below the threshold values. Instead, a more important factor seems to be whether or not the B2 phase is completely encapsulated by a shell of low-Fe compounds Al_8Mn_5 and $Al_{11}Mn_4$ (Fig. 3) that prevent galvanic coupling between B2-Al(Fe,Mn) and α-Mg.

The formation of Al_5Fe_2 at the bottom of the crucible in Mn-depleted regions in this work at 750-850 °C is likely to be the origin of lower limit on the Mn content in AZ91D (0.15 wt.% Mn), since these particles had Al_5Fe_2 on the outer surface of particles, giving an Fe-rich compound in direct contact with α-Mg.

Future research needs to perform micro-galvanic corrosion studies at the microstructure level to more directly link the IMCs microstructures to corrosion rates. The method developed here of saturating small volumes of Mg alloy melts in known quantities of Fe followed by

solidification to generate specific Al-Mn-Fe particle microstructures would be well-suited to such studies.

4 Conclusions

The influence of Fe content on the formation of Al-Mn-Fe IMCs has been investigated in Mg-8.9Al-0.72Zn-0.19Mn (wt.%, AZ91) by holding ~2g samples at 640-850 °C for 4 h in Fe-0.2C crucibles. This corresponds to changing the Fe content from ~10ppm to >100ppm Fe. Four Al-Mn-Fe IMCs were identified depending on the Fe content and the location in the crucible: B2-Al(Fe,Mn), Al_8Mn_5, and $Al_{11}Mn_4$ in the bulk AZ91, and additionally Al_5Fe_2 at the bottom of crucibles. In all cases, these grew together in multiphase particles.

B2-Al(Fe,Mn) was present in samples held at 700°C and higher where it was the first phase to form. Al_8Mn_5 formed after B2-Al(Fe,Mn) and encapsulated the B2-Al(Fe,Mn) as multifaceted polyhedron and octapod morphologies. As the Fe content increased, the B2-Al(Fe,Mn) gradually developed to eight-armed $\langle 111 \rangle$-type dendrites which were less covered by the shell of Al_8Mn_5. Direct contact between B2-Al(Fe,Mn) and α-Mg was observed for the higher holding temperatures of 800-850 °C (corresponding to Fe contents of ~0.01 wt.% and higher).

Al_5Fe_2 was only found at the bottom region of the crucible for samples held at 700-850°C, and grew on B2-Al(Fe,Mn) as a thin layer. Based on thermodynamic calculations, the formation of Al_5Fe_2 is likely to be related to a local depletion in Mn at the bottom of the crucible, probably due to diffusion of Mn into the steel crucible and growth of settled IMC particles. Fe-rich Al_5Fe_2 was in direct contact with α-Mg.

$Al_{11}Mn_4$ was the last IMC to form and grew as $\{010\}$ faceted plates on Al_8Mn_5 and Al_5Fe_2 and, sometimes, B2-Al(Fe,Mn), parallel with $\{110\}_{B2}$ planes of cube-shaped particles or octapods.

Reproducible orientation relationships (ORs) were measured by EBSD between B2-Al(Fe,Mn) and each of Al_8Mn_5, Al_5Fe_2 and $Al_{11}Mn_4$, which also led to interrelated ORs between all IMCs in the multiphase particles. It was shown that these ORs reflect crystallographic similarities between the four IMCs which allows interfaces with good atomic matching.

The micro-galvanic corrosion of AZ91 at different Fe levels seems to be correlated to the intermetallic phase(s) which are in direct contact with the α-Mg matrix. At low iron content, the Fe-rich B2 phase was encapsulated by a low-Fe Al_8Mn_5 shell. With increasing iron content, the Fe-rich phases (B2 and Al_5Fe_2) gradually became in direct contact with the α-Mg. The threshold Fe:Mn content for adequate corrosion performance is found to correlate approximately to where B2-Al(Fe,Mn) first becomes exposed to the α-Mg matrix.

Acknowledgements

The authors gratefully acknowledge the use of characterisation facilities within the Harvey Flower Electron Microscopy Suite, Department of Materials, Imperial College London. This work was partially funded by the UK EPSRC Future LiME Hub (EP/N007638/1) and partially supported by the National Natural Science Foundation of China (51904352).

References

[1] C. Blawert, N. Hort, K. Kainer, AUTOMOTIVE APPLICATIONS OF MAGNESIUM AND ITS ALLOYS, Trans. Indian Inst. Met., 57 (2004) 397-408.
[2] A.A. Luo, Magnesium casting technology for structural applications, Journal of Magnesium and Alloys, 1 (2013) 2-22.
[3] M.P. Brady, W.J. Joost, C. David Warren, Insights from a recent meeting: current status and future directions in magnesium corrosion research, CORROSION, 73 (2017) 452-462.
[4] J. Weiler, A review of magnesium die-castings for closure applications, Journal of Magnesium and Alloys, 7 (2019) 297-304.
[5] J. Hanawalt, Corrosion studies of magnesium and its alloys, Trans AIME, 147 (1942) 273-299.
[6] J.E. Hillis, The Effects of Heavy Metal Contamination on Magnesium Corrosion Performance, SAE Transactions, 92 (1983) 553-559.
[7] G.L. Song, A. Atrens, Corrosion Mechanisms of Magnesium Alloys, Adv. Eng. Mater., 1 (1999) 11-33.
[8] S. Mathieu, C. Rapin, J. Steinmetz, P. Steinmetz, A corrosion study of the main constituent phases of AZ91 magnesium alloys, Corrosion Science, 45 (2003) 2741-2755.
[9] O. Lunder, T.K. Aune, K. Nisancioglu, Effect of Mn Additions on the Corrosion Behavior of Mould-Cast Magnesium ASTM AZ91, CORROSION, 43 (1987) 291-295.
[10] M. Liu, G.-L. Song, Impurity control and corrosion resistance of magnesium–aluminum alloy, Corrosion Science, 77 (2013) 143-150.
[11] O. Lunder, K. Nisancioglu, R.S. Hansen, Corrosion of Die Cast Magnesium-Aluminum Alloys, in, SAE Technical Paper, 1993.
[12] O. Lunder, J. Nordien, K. Nisancioglu, Corrosion Resistance of Cast Mg-Al Alloys, Corrosion Reviews, 15 (1997) 439-470.
[13] R.-c. Zeng, J. Zhang, W.-j. Huang, W. Dietzel, K. Kainer, C. Blawert, K. Wei, Review of studies on corrosion of magnesium alloys, Transactions of Nonferrous Metals Society of China, 16 (2006) s763-s771.
[14] S. Pawar, X. Zhou, G. Thompson, G. Scamans, Z. Fan, The role of intermetallics on the corrosion initiation of twin roll cast AZ31 Mg alloy, Journal of The Electrochemical Society, 162 (2015) C442.
[15] J.D. Hanawalt, C.E. Nelson, G.E. Holdeman, Dow Chemical Co., Removal of iron from magnesiumbase alloys, in, US patent US2267862A, 1941.
[16] L. Peng, G. Zeng, T. Su, H. Yasuda, K. Nogita, C. Gourlay, Al8Mn5 Particle Settling and Interactions with Oxide Films in Liquid AZ91 Magnesium Alloys, JOM, 71 (2019) 2235-2244.
[17] ASTM-International, B94-18 Standard Specification for Magnesium-Alloy Die Castings, in, West Conshohocken, PA, 2018.
[18] T. Chen, Y. Yuan, T. Liu, D. Li, A. Tang, X. Chen, R. Schmid-Fetzer, F. Pan, Effect of Mn Addition on Melt Purification and Fe Tolerance in Mg Alloys, JOM, 73 (2021) 892-902.
[19] M. Esmaily, J. Svensson, S. Fajardo, N. Birbilis, G. Frankel, S. Virtanen, R. Arrabal, S. Thomas, L. Johansson, Fundamentals and advances in magnesium alloy corrosion, Progress in Materials Science, 89 (2017) 92-193.
[20] M. Liu, P.J. Uggowitzer, A. Nagasekhar, P. Schmutz, M. Easton, G.-L. Song, A. Atrens, Calculated phase diagrams and the corrosion of die-cast Mg–Al alloys, Corrosion Science, 51 (2009) 602-619.
[21] G. Zeng, J. Xian, C. Gourlay, Nucleation and growth crystallography of Al8Mn5 on B2-Al (Mn, Fe) in AZ91 magnesium alloys, Acta Materialia, 153 (2018) 364-376.
[22] D.S. Gandel, M.A. Easton, M.A. Gibson, N. Birbilis, CALPHAD simulation of the Mg–(Mn, Zr)–Fe system and experimental comparison with as-cast alloy microstructures as

relevant to impurity driven corrosion of Mg-alloys, Materials Chemistry and Physics, 143 (2014) 1082-1091.
[23] G. Han, X. Liu, Phase control and formation mechanism of Al–Mn(–Fe) intermetallic particles in Mg–Al-based alloys with FeCl3 addition or melt superheating, Acta Materialia, 114 (2016) 54-66.
[24] E. Owen, L. Pickup, I. Roberts, Lattice constants of five elements possessing hexagonal structure, Zeitschrift für Kristallographie-Crystalline Materials, 91 (1935) 70-76.
[25] F. Stein, S.C. Vogel, M. Eumann, M. Palm, Determination of the crystal structure of the ε phase in the Fe–Al system by high-temperature neutron diffraction, Intermetallics, 18 (2010) 150-156.
[26] S. Thimmaiah, Z. Tener, T.N. Lamichhane, P.C. Canfield, G.J. Miller, Crystal structure, homogeneity range and electronic structure of rhombohedral γ-Mn5Al8, Zeitschrift für Kristallographie-Crystalline Materials, 232 (2017) 601-610.
[27] A. Kontio, E. Stevens, P. Coppens, R. Brown, A. Dwight, J. Williams, New investigation of the structure of Mn4Al11, Acta Crystallographica Section B: Structural Crystallography and Crystal Chemistry, 36 (1980) 435-436.
[28] U. Burkhardt, Y. Grin, M. Ellner, K. Peters, Structure refinement of the iron–aluminium phase with the approximate composition Fe2Al5, Acta Crystallographica Section B: Structural Science, 50 (1994) 313-316.
[29] P. Schobinger-Papamantellos, P. Fischer, Neutronenbeugungsuntersuchung der Atomverteilung von Mg17Al12, Naturwissenschaften, 57 (1970) 128-129.
[30] W. Zheng, H. Mao, X.-G. Lu, Y. He, L. Li, M. Selleby, J. Ågren, Thermodynamic investigation of the Al-Fe-Mn system over the whole composition and wide temperature ranges, Journal of Alloys and Compounds, 742 (2018) 1046-1057.
[31] J.W. Xian, L. Peng, G. Zeng, D. Wang, C.M. Gourlay, Al11Mn4 formation on Al8Mn5 during the solidification and heat treatment of AZ-series magnesium alloys, Materialia, 19 (2021) 101192.
[32] L. Peng, G. Zeng, C. Lin, C. Gourlay, Al2MgC2 and AlFe3C formation in AZ91 Mg alloy melted in Fe-C crucibles, Journal of Alloys and Compounds, 854 (2021) 156415.
[33] M. Ellner, The structure of the high-temperature phase MnAl(h) and the displacive transformation from MnAl(h) into Mn5Al8, Metallurgical Transactions A, 21 (1990) 1669-1672.
[34] E. Owen, G. Williams, A low-temperature X-ray camera, Journal of Scientific Instruments, 31 (1954) 49.
[35] M. Guttmann, Diffusive Phase Transformations in Hot Dip Galvanizing, Materials Science Forum, 155-156 (1994) 527-548.
[36] E. McDevitt, Y. Morimoto, M. Meshii, Characterization of the Fe-Al Interfacial Layer in a Commercial Hot-dip Galvanized Coating, ISIJ International, 37 (1997) 776-782.
[37] K.-K. Wang, L. Chang, D. Gan, H.-P. Wang, Heteroepitaxial growth of Fe2Al5 inhibition layer in hot-dip galvanizing of an interstitial-free steel, Thin Solid Films, 518 (2010) 1935-1942.
[38] L. Liu, L. Xiao, J. Feng, L. Li, S. Esmaeili, Y. Zhou, Bonding of immiscible Mg and Fe via a nanoscale Fe2Al5 transition layer, Scripta Materialia, 65 (2011) 982-985.
[39] K.H.J. Buschow, P.G. Van Engen, R. Jongebreur, Magneto-optical properties of metallic ferromagnetic materials, Journal of Magnetism and Magnetic materials, 38 (1983) 1-22.
[40] ASTM-International, B80-15 Standard Specification for Magnesium-Alloy Sand Castings, in, West Conshohocken, PA, 2015.

Figure caption

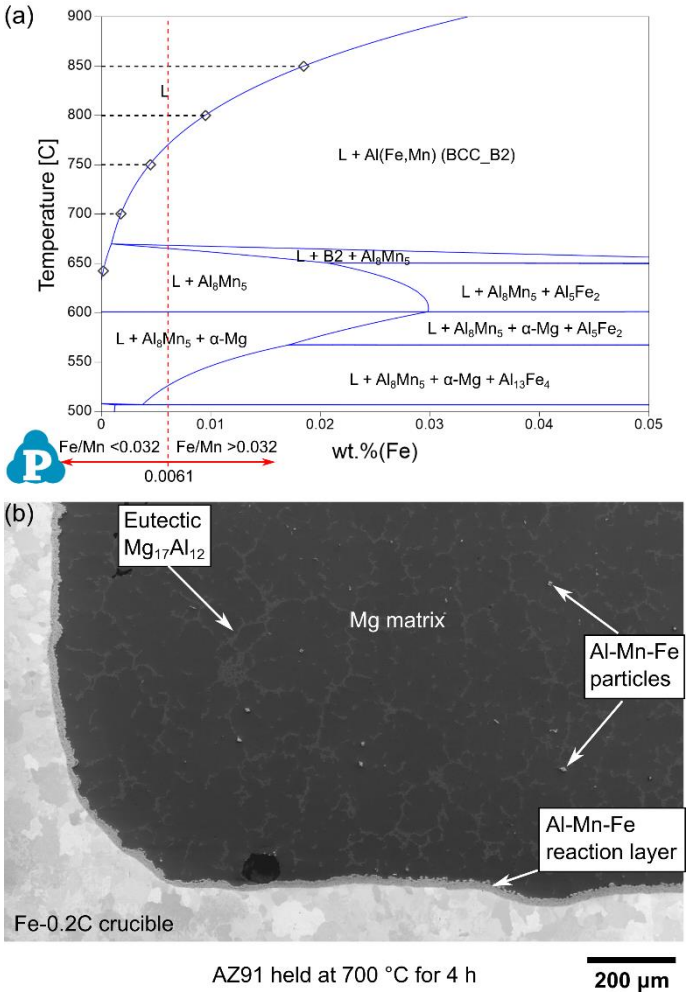

Fig. 1. (a) Equilibrium isopleth section of (90.14-x)Mg-8.95Al-0.72Zn-0.19Mn-xFe calculated in Pandat software with the PanMg2018 database. Black dashed lines represent the saturated Fe content in the melt at different target temperatures = 1, 18, 44, 94, 184 ppm. (b) SE image of the typical microstructure of AZ91 in Fe-0.2C crucible after isothermal holding at 700 °C for 4 h.

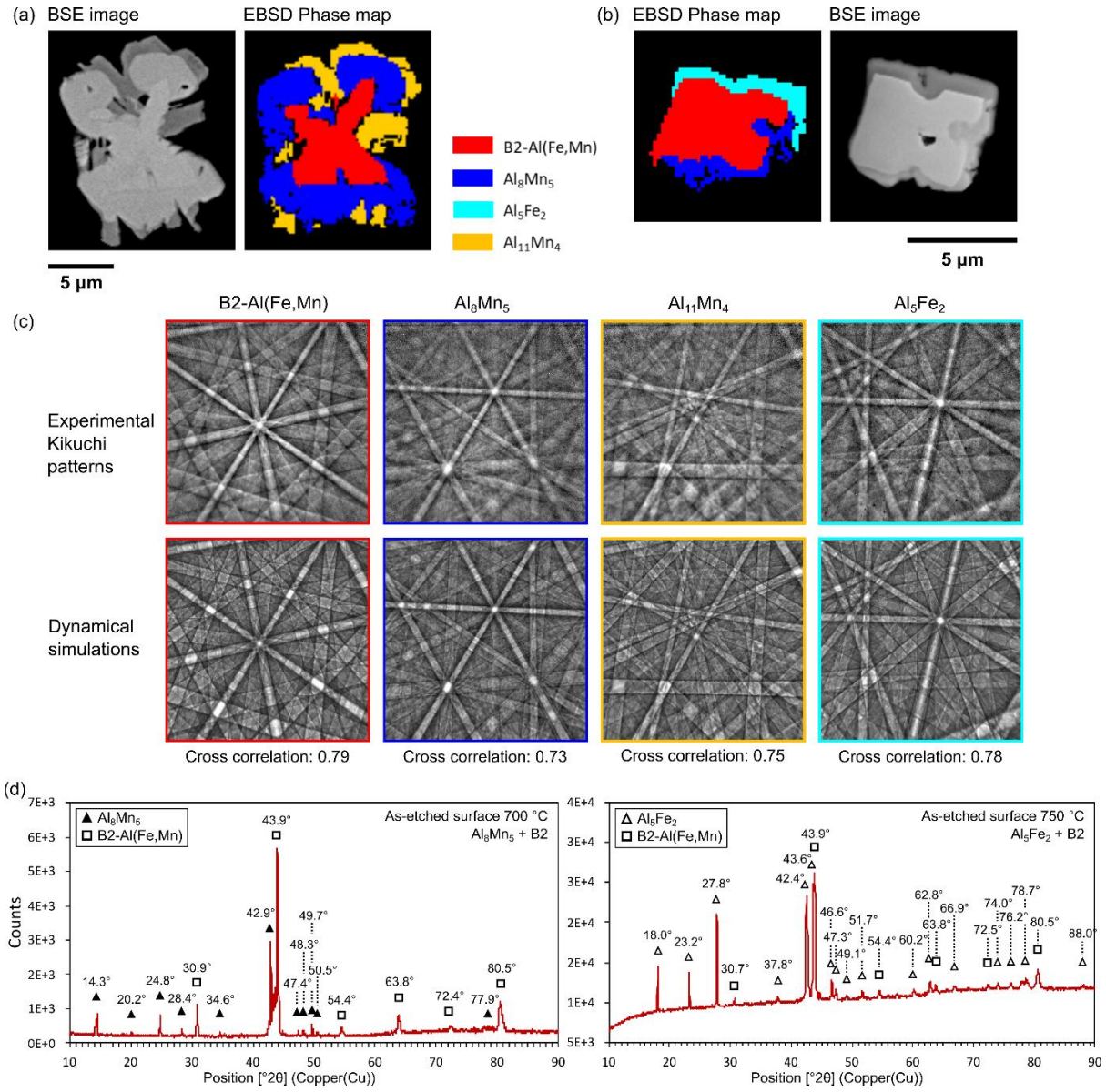

Fig. 2. (a-b) BSE image and EBSD phase map of typical IMC particles (holding at 800 °C for 4 h). (c) Experimental Kikuchi patterns of B2-Al(Fe,Mn), Al_8Mn_5, $Al_{11}Mn_4$ and Al_5Fe_2 from the particles and dynamical simulated patterns with cross correlation coefficients (0-1 = zero similarity-perfect match). (d) XRD diffraction patterns for as-etched surfaces of the reaction layer in 700 and 750 °C samples.

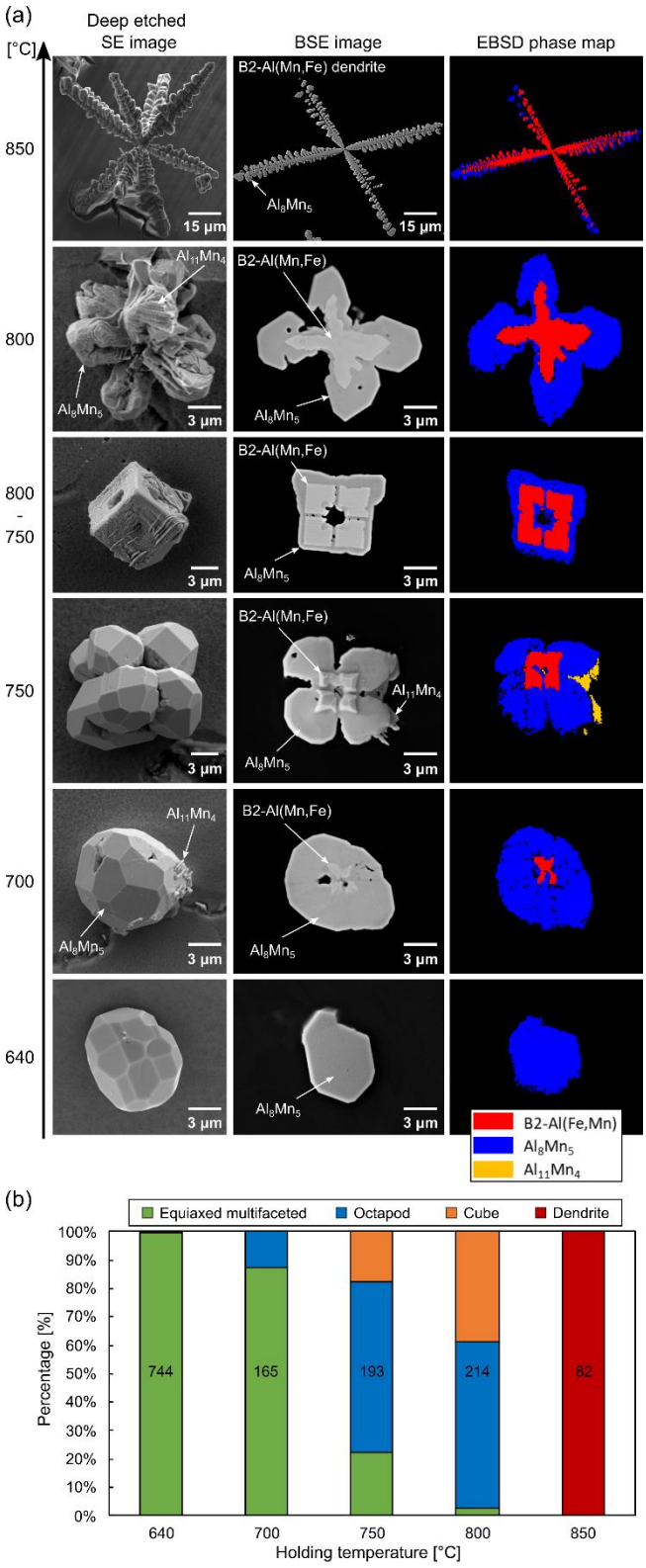

Fig. 3. (a) Typical morphology of Al-Mn-Fe IMCs found in AZ91 held at different target temperatures for 4 h (increasing holding temperature = increasing Fe content in the melt). Left column: SE images of 3-D morphology of particles in deep etched sample. Middle column: BSE images of cross-sectioned particles. Right column: EBSD phase maps corresponding to the cross-section in the middle. (b) Percentage of Al-Mn-Fe IMC particle morphologies at each holding temperature. The total count of measured particles is marked on the bars.

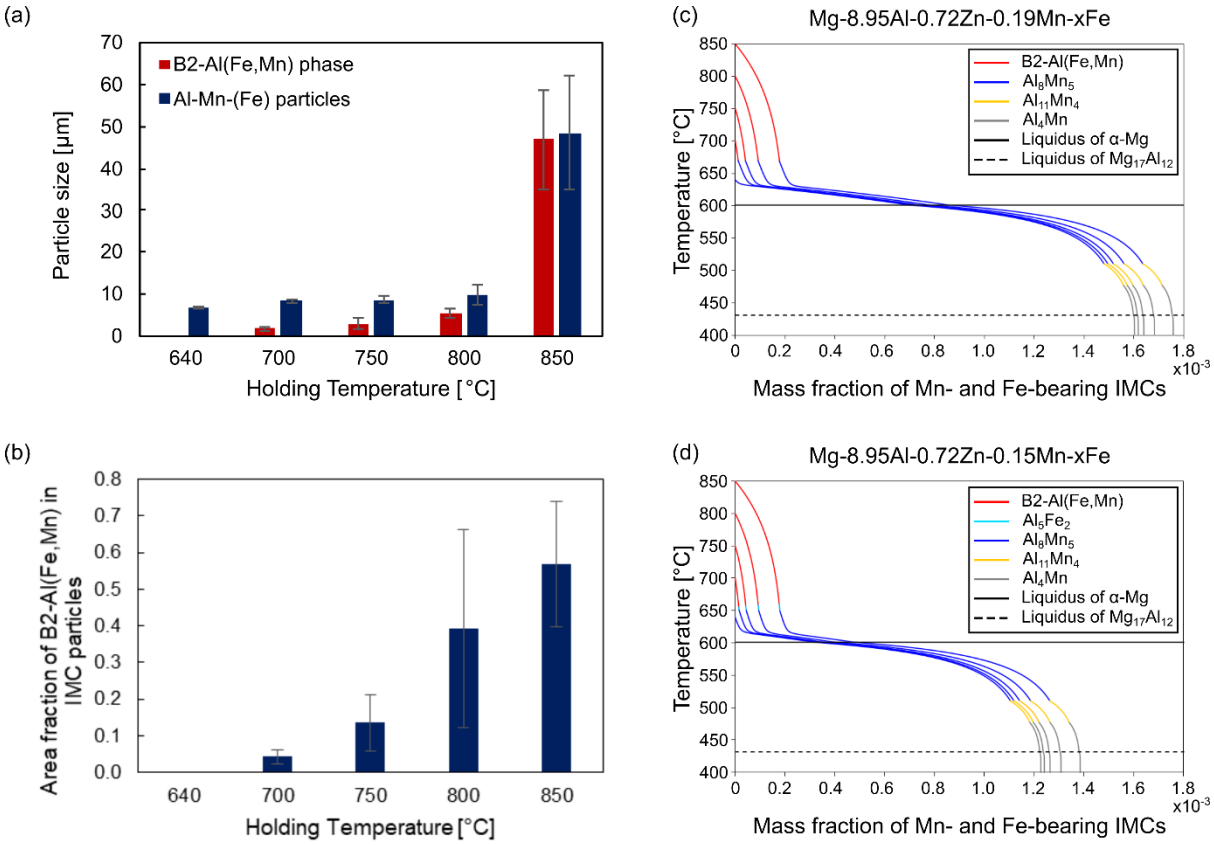

Fig. 4. (a) Particle dimension of B2-Al(Fe,Mn) and total multiphase particles at different holding temperatures. (b) Area fraction of B2-Al(Fe,Mn) to total particle measured in BSE images. (c) Scheil calculation for Mg-8.95Al-0.72Zn-0.19Mn-xFe (this work) with saturated Fe content at 640, 700, 750, 800 and 850 °C, x = 1, 18, 44, 94, 184 ppm. (d) Scheil calculation for Mg-8.95Al-0.72Zn-0.15Mn-xFe with saturated Fe content at 640, 700, 750, 800 and 850 °C, x = 4, 19, 46, 97, 188 ppm. Only Al-Mn-Fe IMCs are shown in (c)-(d).

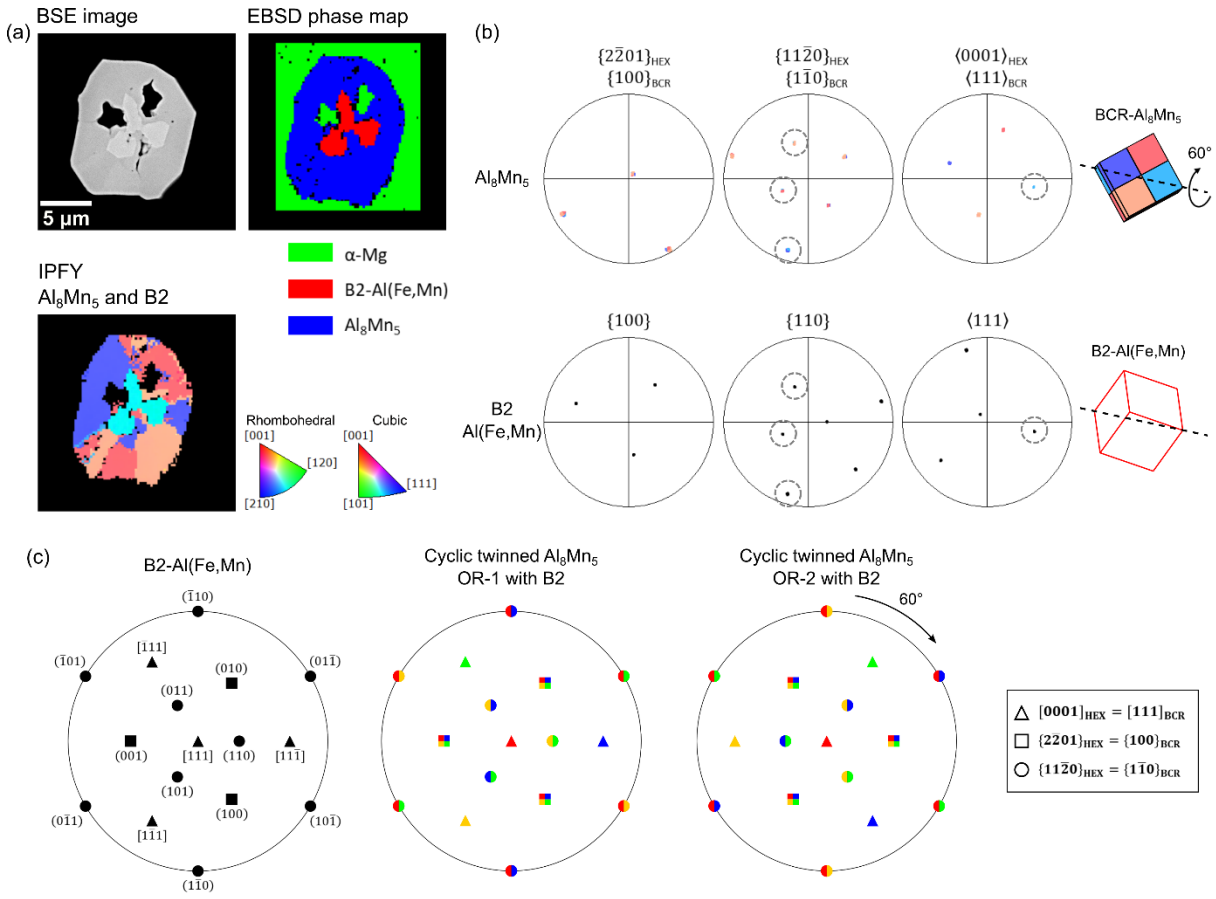

Fig. 5. ORs between Al_8Mn_5 and B2-Al(Fe,Mn). (a) BSE image, EBSD phase map and IPF-Y orientation map (800 °C for 4 h sample). (b) Selected pole figures showing OR-2, and unit cell wireframes of four orientations in the Al_8Mn_5 cyclic twin and B2-Al(Fe,Mn) from the measured Euler angles. (c) Stereographic projection for B2-Al(Fe,Mn) and cyclic twinned Al_8Mn_5 with the $[111]_{B2}$ and the $[111]_{BCR-Al8Mn5}$ of the red Al_8Mn_5 orientation at the centre showing the OR-1 and OR-2.

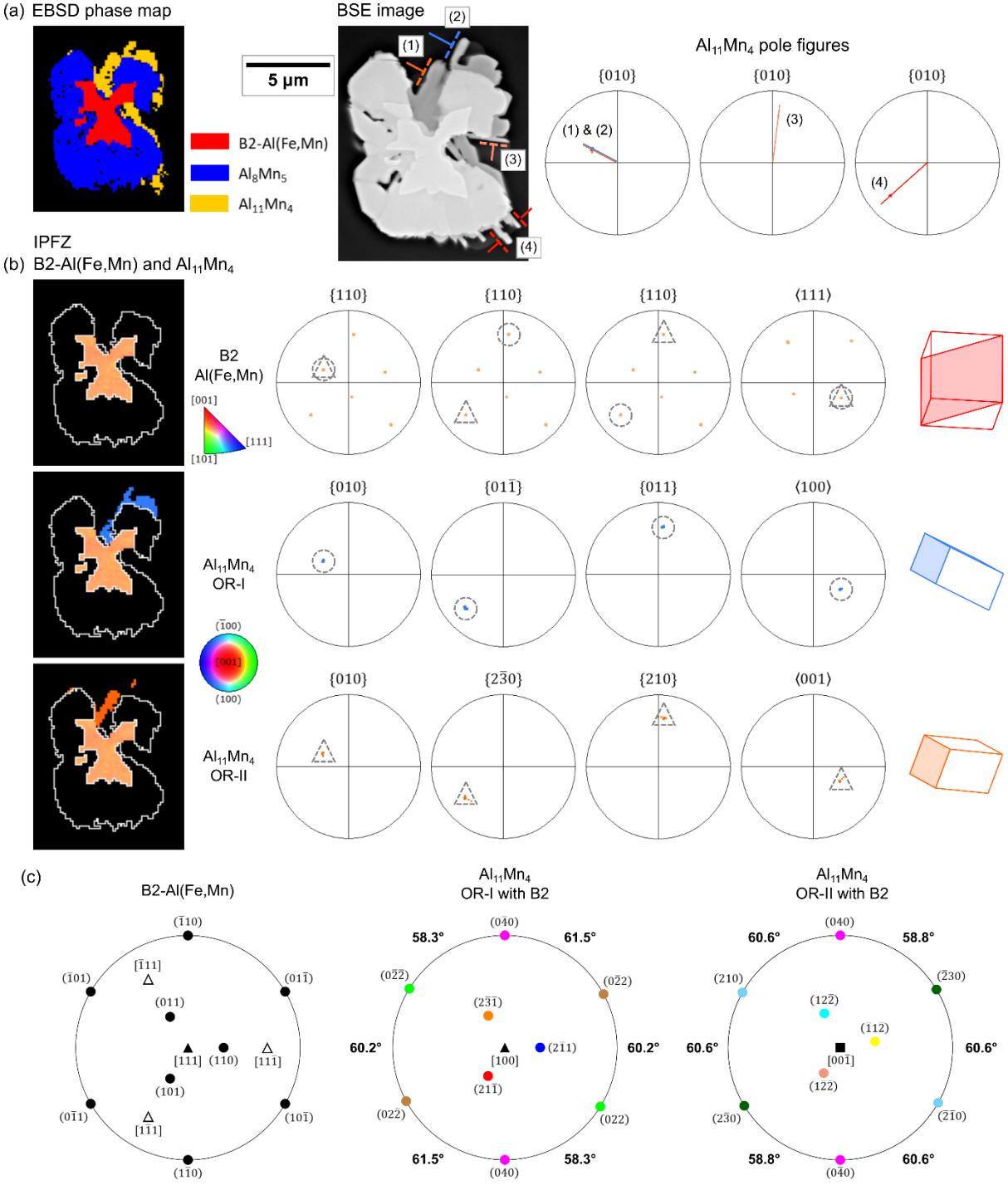

Fig. 6. OR between $Al_{11}Mn_4$ and B2-Al(Fe,Mn) in a sample held at 800 °C for 4 h. (a) EBSD phase map, BSE image, and {010} pole figures of four $Al_{11}Mn_4$ orientations with projected plane normals. (b) IPF-Z orientation map for B2-Al(Fe,Mn) and two $Al_{11}Mn_4$ orientations with OR-I and OR-II, and selected pole figures with highlighted parallel plane normals and direction. (c) Stereographic projections of B2-Al(Fe,Mn) and $Al_{11}Mn_4$ with OR-I and with OR-II.

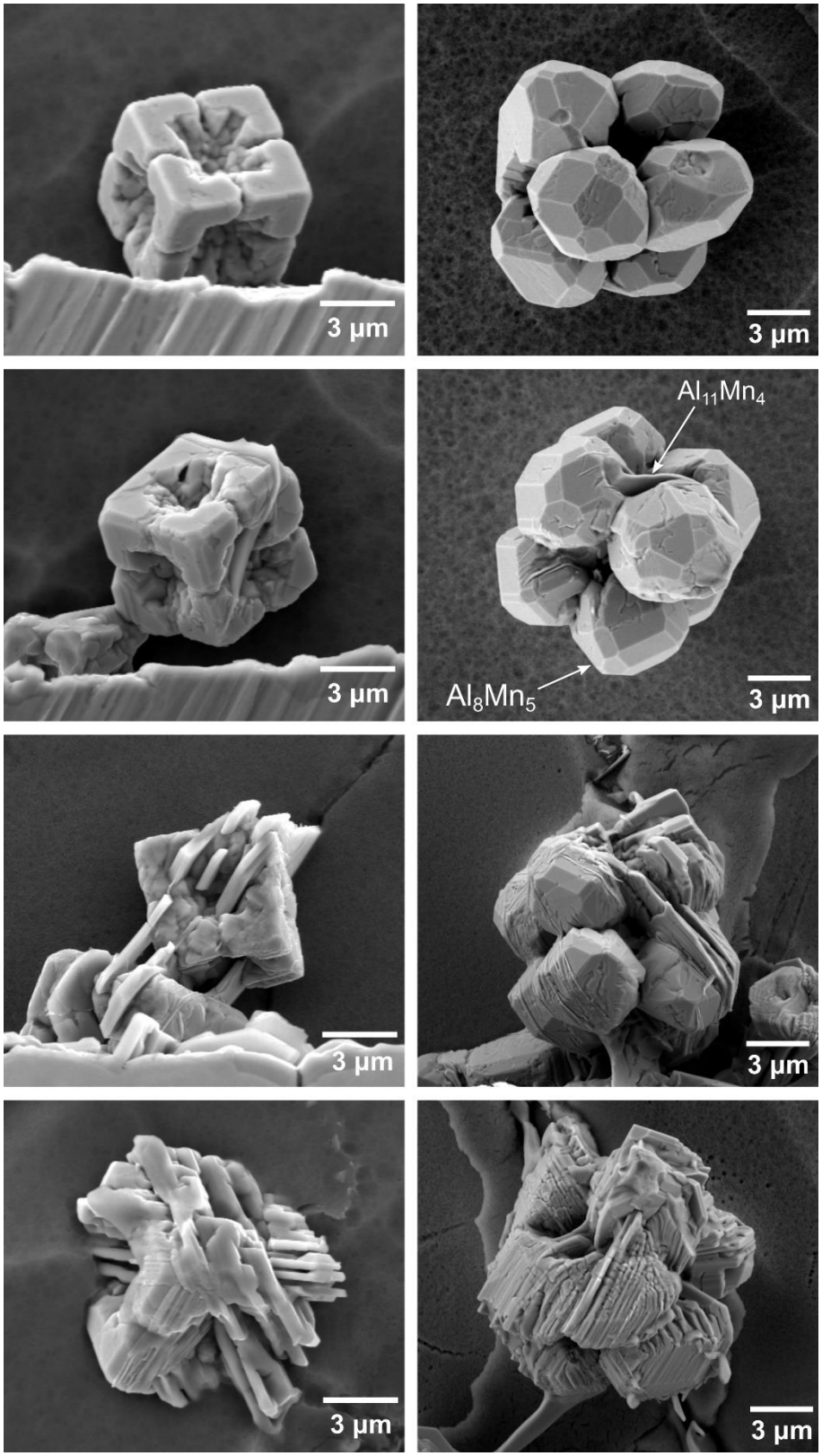

Fig. 7. $Al_{11}Mn_4$ plates on Al-Mn-Fe particles with an increasing degree of $Al_{11}Mn_4$ coverage from top to bottom. Left column: Cube-shaped particles at the bottom of crucible in AZ91 held at 800 °C; Right column: Al_8Mn_5 octapods in the bulk of AZ91 held at 750 °C. $\{010\}_{Al11Mn4}$ plates are parallel with the different members of $\{110\}_{B2}$.

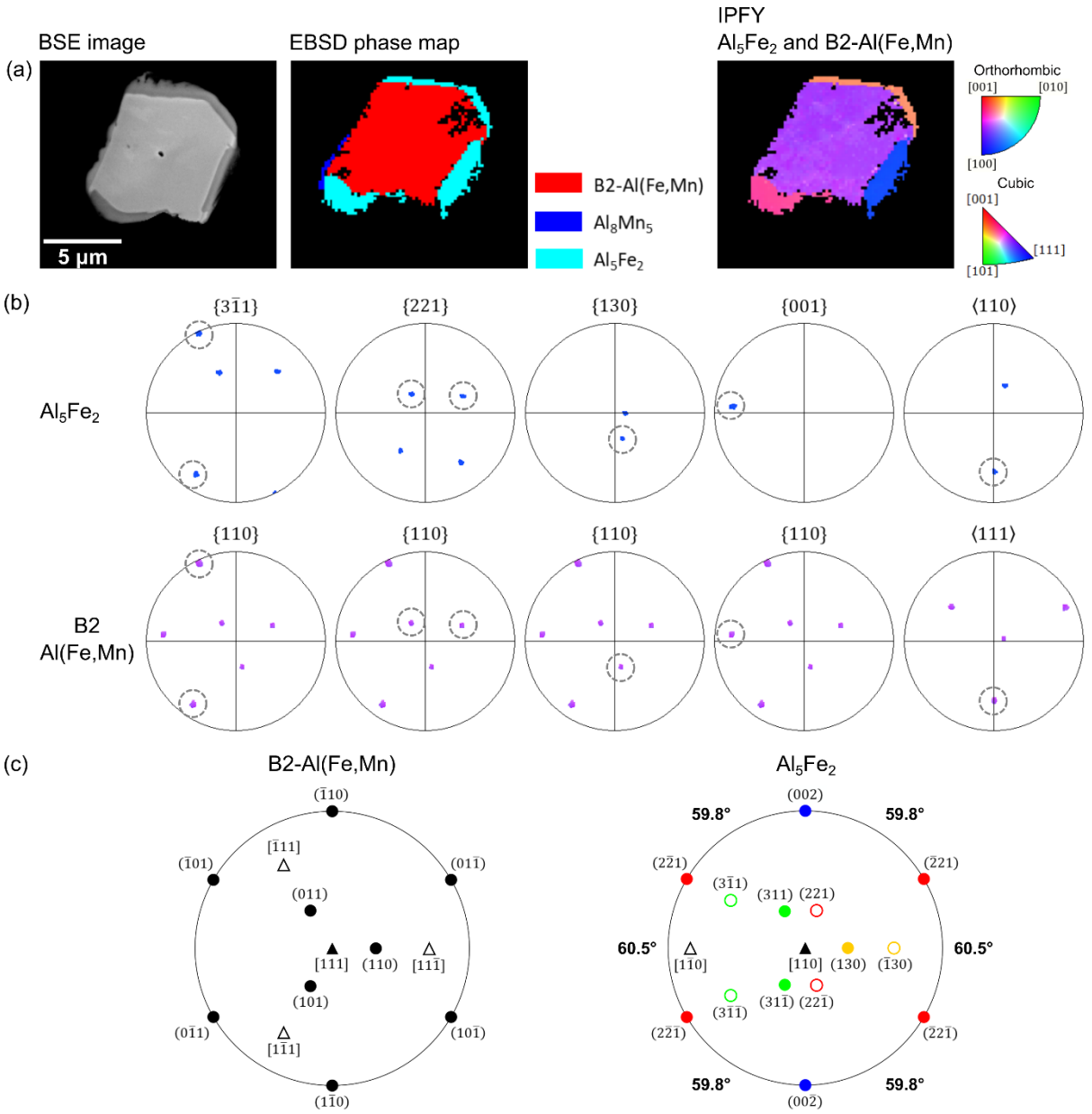

Fig. 8. OR between Al_5Fe_2 and B2-Al(Fe,Mn) in a particle at the bottom of a crucible (800 °C for 4 h sample). (a) BSE image, EBSD phase map and IPF-Y orientation map. (b) Selected pole figures with highlighted parallel plane normals and direction. (c) Stereographic projection of the OR. Filled symbols are near-parallel planes and unfilled symbols are other family members that are not near-parallel in the OR.

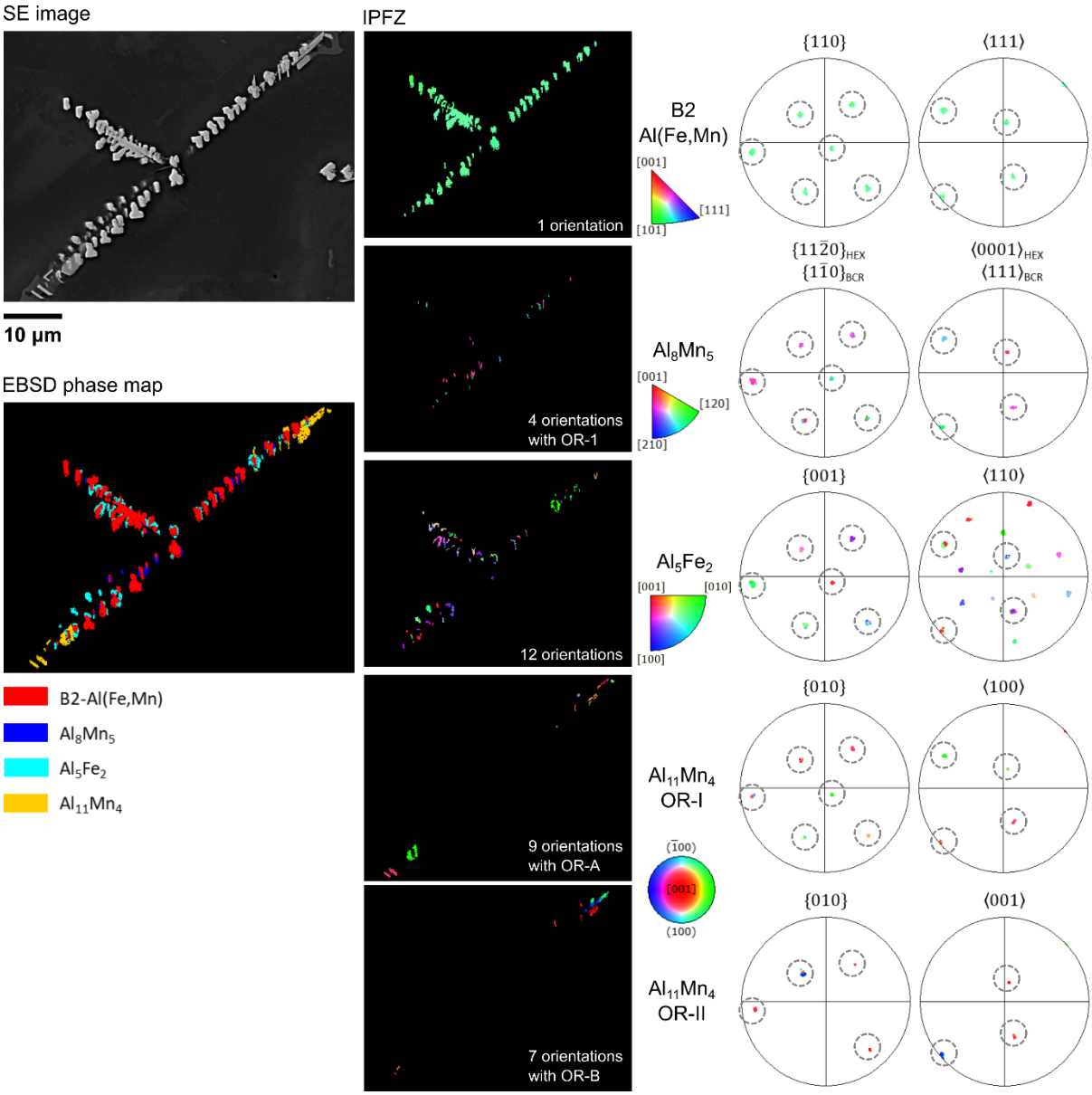

Fig. 9. SE image and EBSD phase map of a typical dendrite at the bottom region of AZ91 held at 850 °C for 4 h. IPF-Z orientation maps are shown for individual phases. Selected pole figures showing multiple orientations all share the same simple ORs among the four IMCs.

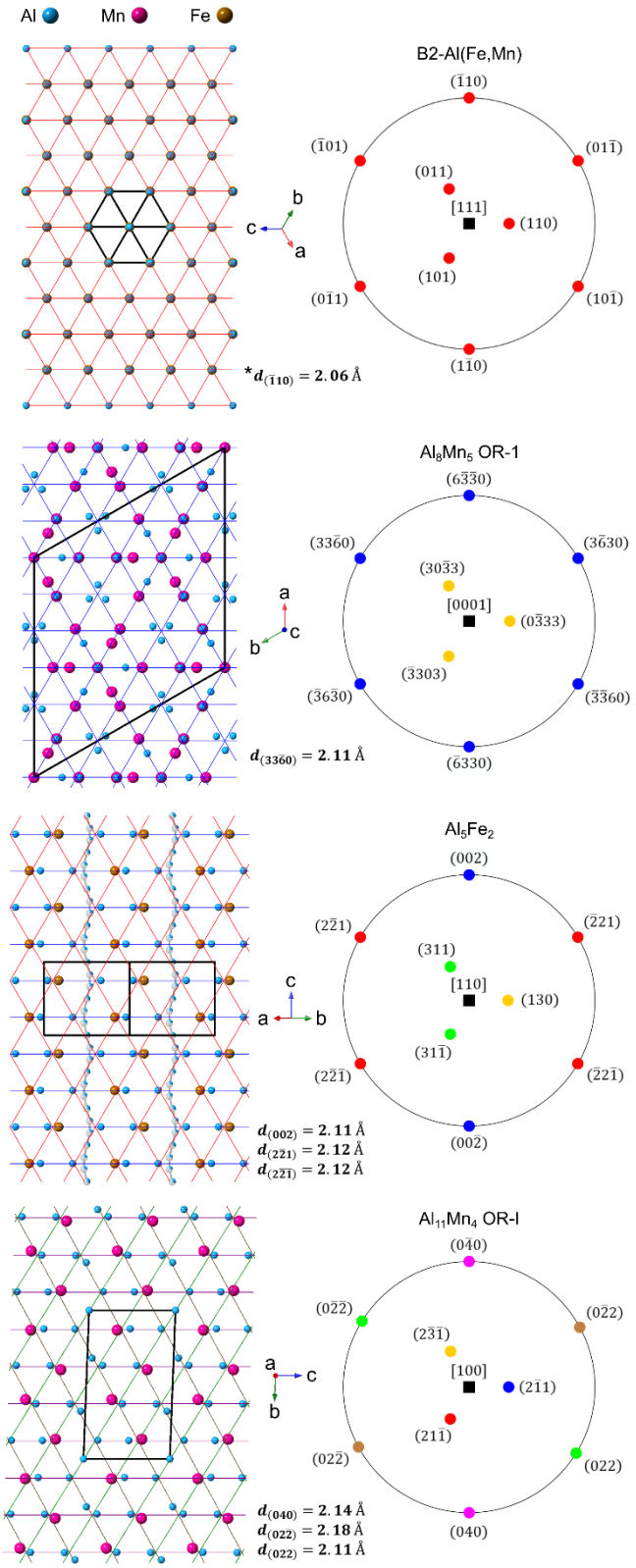

Fig. 10. Comparison of the IMC crystal structures oriented according to the measured ORs. Left column: projection views of atomic structures at the same scale. Unit cells are black. Right column: stereographic projections with the same orientations. Planes from the same family are marked in the same colour. The six planes on the circumference of each stereographic projection are plotted on the atomic projections. The d-spacings of these planes are annotated in the middle.

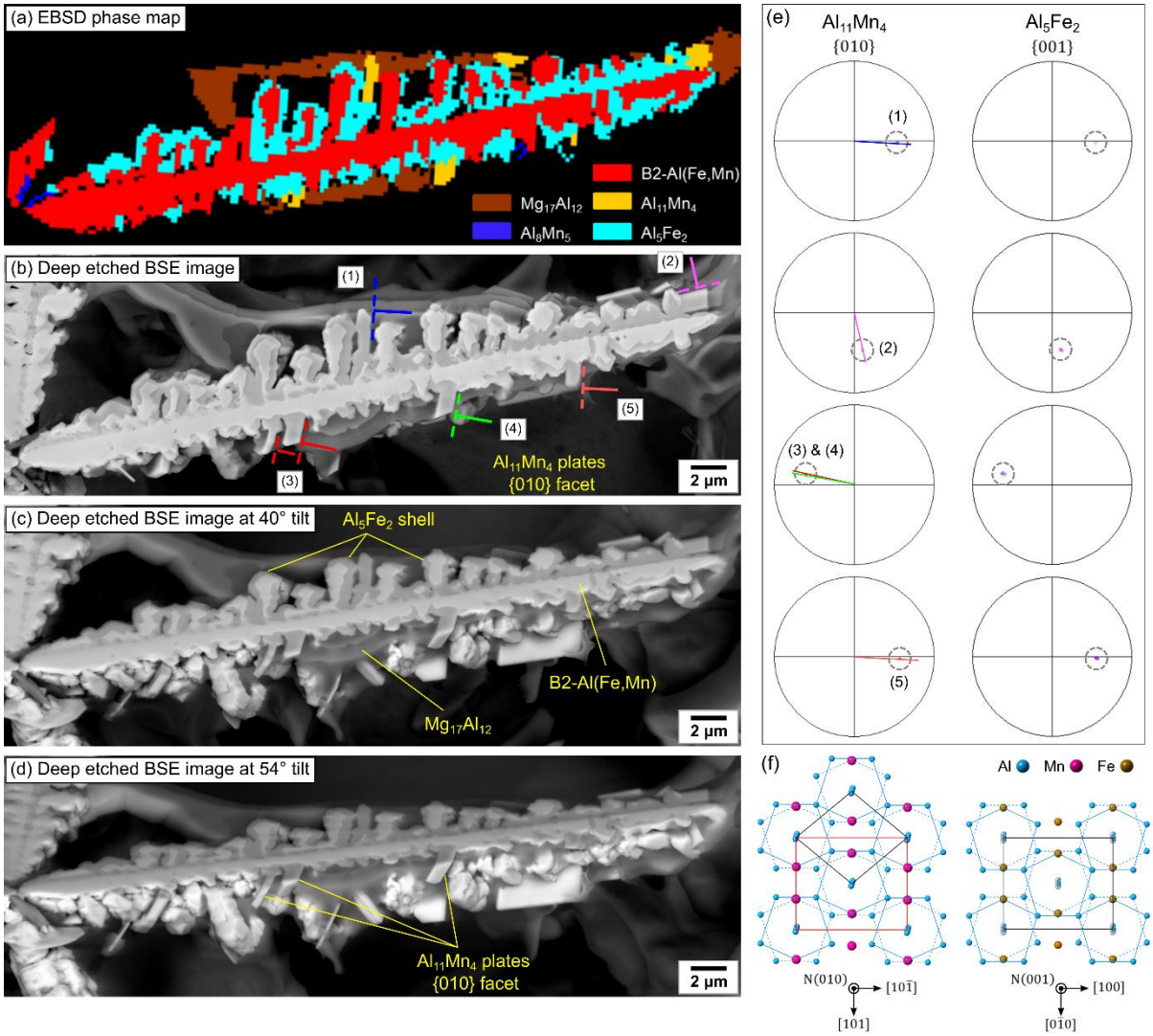

Fig. 11. (a) EBSD phase map of a dendrite arm at the bottom region of an 850 °C for 4 h sample. (b-d) Deep-etched BSE images tilted at 0°, 40° and 54° showing the 3-D morphology. (e) Pole figures of the {010} of $Al_{11}Mn_4$ plates with projected plane normals, and the {001} of the attached Al_5Fe_2. (f) The atomic structure of $Al_{11}Mn_4$ and Al_5Fe_2 at the same scale viewing along the plane normals of the OR; black polygons = unit cells.